Proton elastic scattering at intermediate energies and nuclear densities

H. Sakaguchi

Department of Applied Physics, University of Miyazaki

Proton elastic scattering at intermediate energies is reviewed. After the introduction of the global potential in Dirac phenomenology, relations between Schrödinger potentials and Dirac potentials are explained. Microscopic treatments are compared and modified to explain the scattering precisely in the case of ^{58}Ni. By applying the microscopic treatment neutron density distribution is extracted for the case of ^{120}Sn. Recoiled particle spectrometer is poroposed to measure elastic scattering and to deduce the density distributions of unstable nuclei.

1 Introduction

When we bombard a nucleus with a nucleon or with light ions like deuterons, helium-3, alpha particles, etc., various nuclear phenomena occur, including elastic scattering, inelastic scattering, nucleon transfer reactions and projectile fragmentation, depending on the projectile species and the bombarding energy. The simplest among these phenomena — and at the same time the phenomenon with the smallest amount of internal freedom — is the elastic scattering of a nucleon by a nucleus which we treat in this lecture.

In elastic scattering the target nucleus is not excited. Thus its initial and final states are the same. Furthermore, the initial states in such experiments are the target ground states, the charge distributions of which can be measured precisely by electron scattering. The wave function of the proton part of the target ground state is restricted and almost defined by the experiment. Thus elastic scattering is a good type of reaction to use as a probe of the interactions and the dynamics which occur inside the nucleus. It is quite understandable that the first successful attempt to explain nuclear reactions microscopically began with elastic scattering.

1.1 Microscopic optical potential

When a nucleon enters into the nucleus, the nucleon seems to feel a mean field, because the phenomenological optical potential discussed in the previous section explains the scattering very precisely. In this section we briefly review the microscopic optical potential for energies below 100 MeV. When

we use the word *Microscopic*, it means to explain the nucleon-nucleus elastic scattering from only the superposition of the nucleon-nucleon interaction. If we superimpose the bare nucleon-nucleon interaction, it overestimates the depth of the resultant potentials. If we estimate the imaginary potential from the mean free path derived from the free nucleon-nucleon cross section, we obtain an absorptive potential which is too deep. We need to consider the effects of Pauli-blocking inside the nucleus and also various correlation effects. Because of such effects, the nucleon-nucleon interaction inside the nucleus differs from that in the free space.

The nuclear matter theory developed at the end of 1950's[17] gives us a guideline to construct an effective nucleon-nucleon interaction, namely the G-matrix theory, taking into account the Pauli-blocking effect and the correlation effect in an approximate way. The G-matrix is then folded[25] with the density distributions of protons and neutrons in the nuclear ground state to give a microscopic optical potential. Proton density distributions are estimated from charge distributions, but neutron density distributions are only inferred from model calculations, such as Hartree-Fock calculations with the simplified interactions or from various assumptions.

There exist some problems involved in using the microscopic optical potential. In particular, there are problems with the imaginary part of the mean field, which do not appear in the binding energy case. If the incident energy of the nucleon is so high that quasi-free scattering is the main source of the imaginary part, the above formula for the mean field will be a good approximation. However, if the incident energy of the projectile is sufficiently low and the collective excitations or the process of the compound nucleus formation occupy the larger part of the reaction, the approximation given above becomes less accurate. Thus for comparison of the microscopic theory with experimental data, calculations employing a renormalized imaginary part are often used.

Experimental data for E_n =21.3 MeV[23] along with the microscopic calculation[20]' [21]. For the solid curves in Fig. 4, both the depths of the real and imaginary parts of the optical potential are renormalized. However, at higher energy, for example at $E_p = 65$ MeV they are not renormalized[21].

These nonrelativistic treatments have been applied to the scattering below 100 MeV of proton energy. In order to explain the real scattering, these microscopic optical potential have to be renormalized. Especially the imaginary part of the microscopic optical potential have to be multiplied by the normalization factor, since these microscopic approaches do not take into account the collective excitation, which important at the low incident energy.

1.2 Scattering at intermediate energies

At intermediate energies nuclear reaction mechanism becomes simpler, since the velocity of the projectile is much faster than the fermi motion of the bound nucleons. The main part of the reaction cross section is governed by the quasi-free scattering. Thus we expect to treat even the imaginary part of the optical potential by microscopic theories. If we can treat the scattering microscopically, we can deduce the wave fuction or density distribution of the target ground state.

Elastic scattering of protons has been successfully employed as a probe to discern various microscopic approaches to nuclear interactions. The ground state wave function of the target nucleus used for elastic scattering is restricted by the charge distribution measured by electron scattering. Thus ambiguities due to the nuclear structure are relatively small for the elastic scattering. Moreover, the mean free path of intermediate energy protons in nuclear matter is large enough to penetrate into the nucleus, thus providing some sensitivity to the nuclear interior. Therefore, a considerable number of works have been devoted to proton elastic scattering to determine interactions and nuclear structures even in the nuclear interior.

For unstable nuclei we could apply the nuclear interactions confirmed in the scattering of stable nuclei to deduce the nuclear densities.

In early years these researches have based on nonrelativistic approaches. However since 1980s, the relativistic approaches based on Dirac equations have been applied to the elastic scattering of intermediate energy protons, and have successfully explained the scattering, especially polarization observables. For example, analysis on the elastic scattering of $180\,\mathrm{MeV}$ polarized protons by $^{40}\mathrm{Ca}$[1] has shown that the combination of strong attractive scalar and strong repulsive vector potentials in the Dirac equation has led to a moderate but unusual "wine-bottle" shape of Schrödinger potential, which had been used in some earlier analysis. The Dirac equation have been employed but the potentials used in the analysis have been phenomenological Woods-Saxon type functions. Clark et al. have extended the Dirac phenomenology and finally released the "Global potentials"[2], which have been able to explain elastic proton scattering off spin zero nuclei from $20\,\mathrm{MeV}$ to $1040\,\mathrm{MeV}$ for $^{12}\mathrm{C}$ to $^{208}\mathrm{Pb}$ targets.

In order to relate the scattering to the ground state wave function, we need to have a more fundamental and microscopic approach to the scattering. McNeil, Shepard and Wallace[3] who also have found a dramatic improvements for spin dependent observables for $^{16}\mathrm{O}$ and $^{40}\mathrm{Ca}$ at $500\,\mathrm{MeV}$ by using the Dirac equation. They have applied impulse approximation to the Dirac approach, and determined directly from nucleon–nucleon (NN) phase shifts.

Following the success of this relativistic impulse approximation (RIA), Murdock and Horowitz[4, 5] have calculated the elastic scattering off ^{16}O, ^{40}Ca and ^{208}Pb between 200 and 400 MeV using the RIA and obtained qualitative agreement with experimental data, especially polarization observables.

2 Relativistic impulse approximation

In the intermediate energy region the impulse approximation is thought to describe the elastic and quasi-elastic scattering of protons qualitatively, because here the velocity of the projectile is much larger than the velocity of Fermi motion of the nucleon in the nucleus. The word of relativistic means the application of impulse approximation to the Dirac approach. Namely, in the relativistic impulse approximation (RIA), the mean field is obtained directly by folding the nucleon-nucleon interaction in the relativistic formalism with the density distribution. Thus the RIA seems to relate the coupling constants and the masses of the exchanged mesons directly to nuclear reactions. By using the RIA formalism, we can now investigate the medium effects of the nucleon-nucleon interaction inside the nucleus. Our analysis is essentially based on the relativistic impulse approximation (RIA) of Murdock and Horowitz (MH model)[4] because of its simpleness. Anyway in order to describe the scattering we need to modify the interaction in a reasonable way. In the MH model, an NN scattering amplitude of the relativistic Love-Franey model of the form

$$
\begin{aligned}
F &= F^S + F^V \gamma^\mu_{(0)} \gamma_{(1)\mu} - F^{PV} \frac{\slashed{q} \gamma^5_{(0)}}{2M} \frac{\slashed{q} \gamma^5_{(1)}}{2M} \\
&\quad + F^T \sigma^{\mu\nu}_{(0)} \sigma_{(1)\mu\nu} + F^A \gamma^5_{(0)} \gamma^\mu_{(0)} \gamma^5_{(1)} \gamma_{(1)\mu},
\end{aligned}
\tag{1}
$$

is used. Here the subscripts (0) and (1) refer to the projectile and target nucleons, respectively. The superscripts S, V, PV, T, and A designate scalar, vector, pseudo-vector, tensor and axial-vector parts of the NN amplitude. Note that the pseudo-scalar piece $F^{PS} \gamma^5_{(0)} \gamma^5_{(1)}$ is replaced by the pseudo-vector one in (1). They are equivalent for free NN scattering, but may be different in a nucleus. Indeed pseudo-vector coupling is desirable to give meaningful agreements at lower energies[4, 5].

Each of $F^L (L = S, V, PV, T$ or $A)$ may be written in the MH model as

$$
F^L(q, E_c) = i \frac{M^2}{2E_c k_c} \left[F^L_D(q) + F^L_X(Q) \right],
\tag{2}
$$

$$
F^L_D(q) = \sum_j \delta_{L,L(j)} \{\vec{\tau}_0 \cdot \vec{\tau}_1\}^{I_j} f^j(q),
\tag{3}
$$

$$
F^L_X(Q) = (-1)^T \sum_i B_{L(j),L} \{\vec{\tau}_0 \cdot \vec{\tau}_1\}^{I_j} f^j(Q),
\tag{4}
$$

$$
f^j(q) = \frac{g_j^2}{q^2 + m_k^2} \left(\frac{\Lambda_j^2}{\Lambda_j^2 + q^2} \right)^2 - \frac{\bar{g}_j^2}{q^2 + \bar{m}_k^2} \left(\frac{\bar{\Lambda}_j^2}{\bar{\Lambda}_j^2 + q^2} \right)^2,
\tag{5}
$$

where D and X indicate the direct and exchange terms. , q and Q are direct and exchange three-momentum transfers. I_j and $L(j)$ denotes the

j-th meson's isospin and Lorentz type of coupling to nucleon. $B_{L(j),L}$ is the $(L(j), L)$ component of the Fierz transformation matrix. The coupling constant, mass and cut-off parameter for the j-th meson denoted by g_j, m_j and Λ_j are fitted to the free NN amplitudes at several different laboratory energies. The full set of parameters can be found in Ref. [4, 5]. These NN amplitudes are folded with scalar ,vector and tensor densities to give Dirac mean fields.

In general a tensor potential U^T has to be included even for a spin zero nucleus, however, it is found to be small and neglected in this model. Thus the Dirac equation for the projectile is written as

$$\left\{ -i\vec{\alpha} \cdot \vec{\nabla} + U^V(r; E) + \beta \left[M + U^S(r; E) \right] \right\} \mathcal{U}_0(r) = E\,\mathcal{U}_0(r). \qquad (6)$$

Here $\mathcal{U}_0$ is the incident projectile wave function, E is the total energy in nucleon–nucleus cm coordinate system, and M is the mass of the proton, $\vec{\alpha}, \beta$ are Dirac matrices. Coulomb potential should be included into U^V. The scattering observables, cross sections, analyzing powers and spin rotation parameters, are obtained by solving the Dirac equation.

3 Comparison with various microscopic models

First we compare our experimental data with the RIA calculations of Murdock and Horowitz [32] (MH). The solid curves in Fig. 1, 2 represent the RIA calculations with the Pauli-blocking effect correction used in the method of MH .

The density distributions (vector and scalar densities for protons and neutrons) used for the ^{58}Ni target nuclei were calculated using the relativistic Hartree (RH) approximation of Horowitz and Serot. These are shown in Fig. 3.

Although the solid curves in Fig. 1, 2 reproduce the analyzing power precisely, the angular distributions of the cross section are poorly reproduced, especially at backward angles (larger than $30°$), where the momentum transfer is more than 2 fm^{-1}. Since cross sections at forward angles, where the Rutherford scattering is the dominant mechanism, are reproduced quite well by the calculation, the ambiguity in the absolute value of the experimental cross section is small. This tendency is the same for all three energies. The dashed curves in the figure represent the calculation employing the RIA IA2 by Tjon and Wallace. The density distribution was calculated with the RH approximation using the parameter TM2 of Toki et al., which is capable of
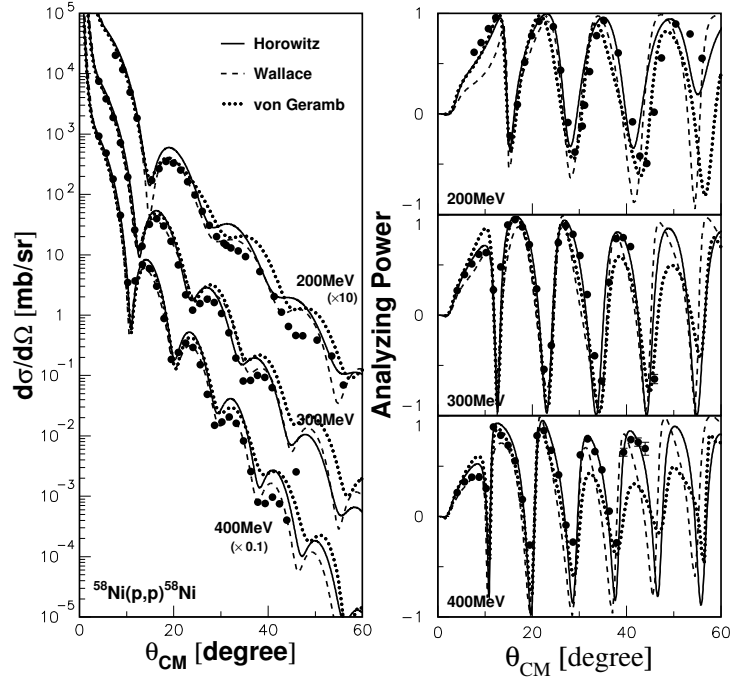
6

Figure 1: The experimental data of cross sections and analyzing powers of proton elastic scattering from ^{58}Ni at 200, 300 and 400 MeV indicated by solid circles are compared to original (unmodified) impulse approximation models. The solid lines and dashed lines indicate the relativistic impulse approximations of Horowitz *et al.* and Wallace *et al.*, respectively. The dotted lines represent the nonrelativistic microscopic optical potential calculations using the G-matrix of von Geramb. None of these models satisfactorily explain the experimental data, especially angular distributions of cross sections.
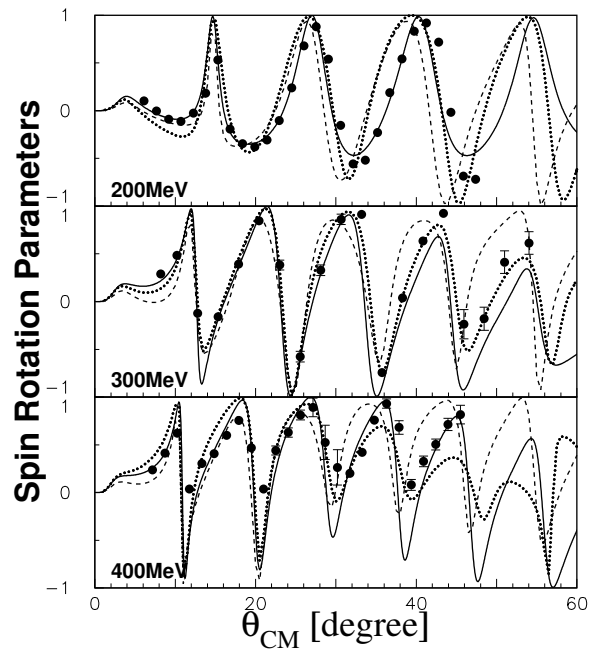
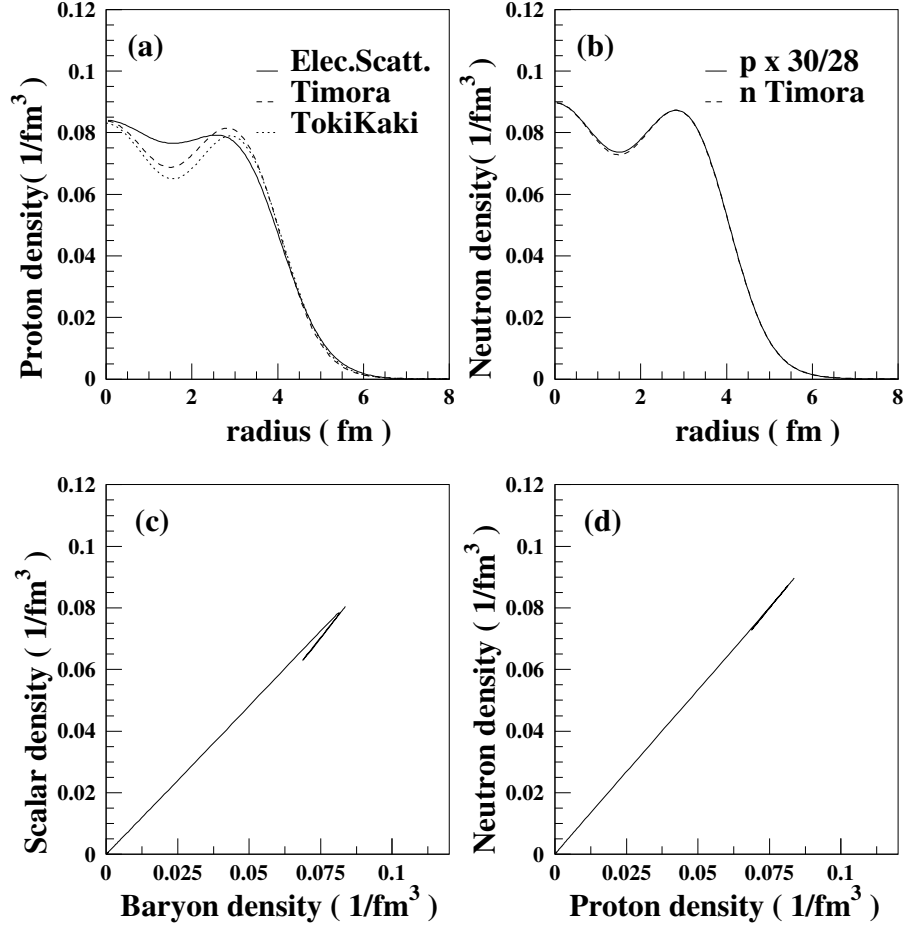Figure 2: Same as Fig. 1, but for spin rotation parameters.

Figure 3: Various densities used in the RIA calculations. (a) Point proton densities are shown. The solid curve is a density distribution deduced from the charge distribution measured by electron scattering. The dashed curve represents the proton density determined by the relativistic Hartree calculation of Horowitz and Serot. The dotted curve represents a relativistic Hartree calculation performed by Kaki with different parameters and the nonlinear meson field of Toki. (b) Relative shapes for the point proton and the point neutron distribution are compared. The solid curve is the calculated point proton distribution multiplied by 30/28, which is equal to the neutron distribution, assuming the proton and neutron distributions are the same. The dotted curve is the neutron distribution calculated using the relativistic Hartree code. (c) The baryon density for protons and the scalar density for protons are compared for the ^{58}Ni nucleus. (d) The baryon densities for protons and neutrons are compared for the ^{58}Ni nucleus.

reproducing even the density distribution of unstable nuclei[?]. The TM2 parameter gives almost the same baryon density as the calculation of Horowitz and Serot as indicated by the dotted curve in Fig. 3a. The IA2 calculation reproduces the experimental results at 400 MeV quite well, except at backward angles. At 192 MeV and 295 MeV it overestimates the cross section, as shown in Fig. 1, 2. The predicted analyzing powers deviate from those observed experimentally at 192 MeV. The IA2 model seems to predict the cross sections better than the approach of MH at all three energies. However with regard to the analyzing power the IA2 prediction is worse than that of MH. The dotted curves in Fig. 1, 2 represent the calculation of the scattering using a non-relativistic Schröedinger type optical potential. We have calculated the non-relativistic Schrödinger optical potential using the G-matrix of von Geramb[37], following the procedure of Rikus and von Geramb[?]. The density distribution used was obtained by unfolding the free proton charge form factor from the charge distribution of the sum of Gaussian type[?] deduced from electron scattering experiments. At 192 MeV the non-relativistic optical potential explains the experiments fairly well, providing a description nearly equivalent to that provided by the RIA approaches. It also overestimates the cross section at backward angles. For Ay the prediction deviates from the experiments even at 192 MeV. In general, as the incident energy increases, the deviation between the prediction given by the method of von Geramb and the experimental values increases. In particular, this deviation is large in analyzing powers at 400 MeV. In summary, none of the three models listed above can satisfactorily explain the experimental data. This is true in particular with regard to differential cross section data. Among the three models, only that of MH explains the analyzing power precisely.

Since cross sections at forward angles, where the Rutherford scattering is the dominant mechanism, are reproduced quite well, the ambiguity in the absolute value of the cross section is small.

4 Tuning the medium effect parameters in nuclei

In order to explain the scattering we need to modify the NN scatteing amplitudes by especially in the nuclear interiaor. For the calibration of the effective nucleon-nucleon interaction we use the scattering from the nucleus, whose density distribution is well known.
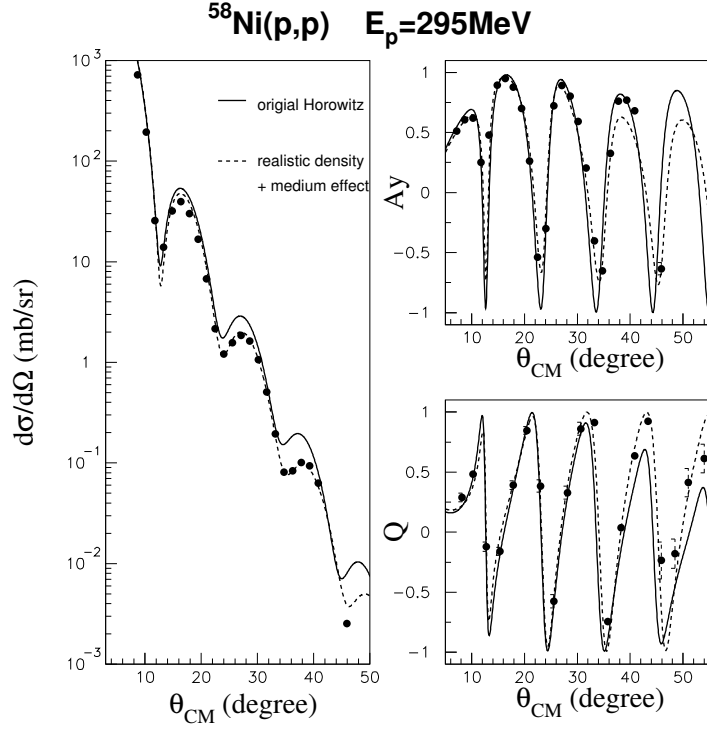
Fig.4 ^{58}Ni(p,p) at E$_p$=300 MeV and the RIA calculations. Broken curves are RIA with the medium effect and the solid curves are original calculation by the code of Horowitz[ref.2]

We used elastic scattering from ^{58}Ni to tune the interaction, since ^{58}Ni is the heaviest stable nucleus with N $\approx$ Z and the density distribution of neutrons in ^{58}Ni is well assumed to be the same as the one for protons. The relativistic Hartree (RH) calculation predicts the same shape for proton and neutron density distributions. In the density matrix expansion for the nonrelativistic Hartre Fock calculation the difference of the root mean square radii of neutron and proton distributions is calculated to be 0.00fm. Thus our assumption is thought to be reasonable. In the RIA calculation we need scalar densities both for protons and neutrons, which are assumed to be 0.96 times of usual densties (vector densities). In the RH calculation for the medium and heavy nuclei the ratio of scalar to vector densities is well approximated to be 0.96.

The result of the RIA calculation is compared with our experimental data [ref.1] in Fig.3. Solid curves are the original Horowitz type calculations, which deviate from the experimental cross section data. In order to explain the experiment we have found that we have to modify the scattering amplitudes

11

of 'Relativistic Love-Franey Interaction'[ref. 2] inside the nucleus as follows;

$$g_j^2, \quad \bar{g}_j^2 \quad \longrightarrow \quad \frac{g_j^2}{1 + a_j\left(\frac{\rho(r)}{\rho_0}\right)}, \qquad \frac{\bar{g}_j^2}{1 + \bar{a}_j\left(\frac{\rho(r)}{\rho_0}\right)}$$

$$m_j, \quad \bar{m}_j \quad \longrightarrow \quad m_j\left(1 + b_j\left(\frac{\rho(r)}{\rho_0}\right)\right), \; \bar{m}_j\left(1 + \bar{b}_j\left(\frac{\rho(r)}{\rho_0}\right)\right), \quad j = \sigma, \quad \omega.$$

Thus we have changed phenomenologically the masses of exchanged mesons and the coupling constants, depending on the nuclear densities, which is called medium effects. Then we can explain the scattering precisely as shown in the broken curves in Fig.3. The form of density dependence is explained as follows by Kohmura[ref.4]. The medium effect of exchanged mesons is considered to be the change of the mass operator of meson propagator.

$$\frac{g_j^2}{q^2 + m_j^2} \longrightarrow \frac{g_j^2}{q^2 + m_j^2 + \Pi_j}, \quad \Pi_j = a_j\left(\frac{\rho}{\rho_0}\right) + b_j\left('\frac{\rho}{\rho_0}\right)q^2 + .. \qquad (7)$$

Here the additional term Π_j in the above meson propagator is introduced as a medium effect. If we expand Π_j in terms of the density ρ and the square of the transfered momentum q^2 , we have

$$\frac{g_j^2}{q^2 + m_j^2 + \Pi_j} \approx \left(\frac{g_j^2}{1 + b_j(\frac{\rho}{\rho_0})}\right)\left(\frac{1}{q^2 + m_j^2 + (a_j - b_j)(\frac{\rho}{\rho_0})}\right). \qquad (8)$$

The medium effect is thought to be one of the presentations for the partial restoration of chiral symmetry, Pauli- blocking, and multi-step processes.

5   Application of medium effects

In the previous section we have tuned the interaction in the RIA with the experimental data by introducing the medium effect. If this medium effect is a global one, we can predict the proton elastic scattering by using known density distributions and the same medium effect parameters as for ^{58}Ni. As an example we compare the proton elastic scattering data for ^{208}Pb measured at TRIUMF[ref. 5] with the RIA modified by the medium effect in Fig 4. The solid curves are the results of the original Horowits type calculation. If we adopt the point
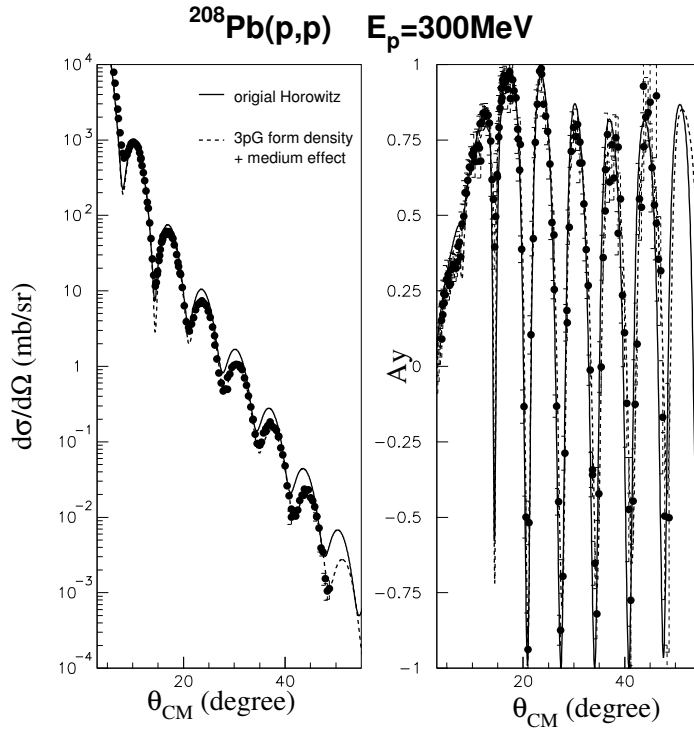
Fig.5 ^{208}Pb(p,p) data of TRIUMF and the predicton by using the medium effect(the broken curve)

proton distribution unfolded from the charge distribution, the neutron density distribution measured at LAMPF and use the same medium effect parameters as in ^{58}Ni, the result of RIA calculation explains the scattering as shown by the broken curves remarkably. In this calculation there is no free parameter to tune the calculation. Thus we have confirmed the applicabilty of our medium effect. Since we now know the interaction, we can determine the density distribution from the scattering. In the case of stable nuclei we know already the density distribution of protons. Then we can deduce the neutron density distributions from the proton elastic scattering.

6 Measurements of proton elastic scattering for Tin isotopes

We have performed a new experiment to measure the neutron density distributions of tin isotopes. In a naive shell model the $3s_{\frac{1}{2}}$ neutron orbit in ^{120}Sn is closed. We have measured differential cross sections and analyzing

powers of proton elastic scattering off ^{116,118,120,122,124}Sn at $E_p = 300$ MeV. The experiment was performed at the Research Center for Nuclear Physics, using the Grand Raiden spectrometer and the focal plane detector system. In order to achieve an accurate measurement of relative cross sections we have installed a newly developed rapid target changer, which can change
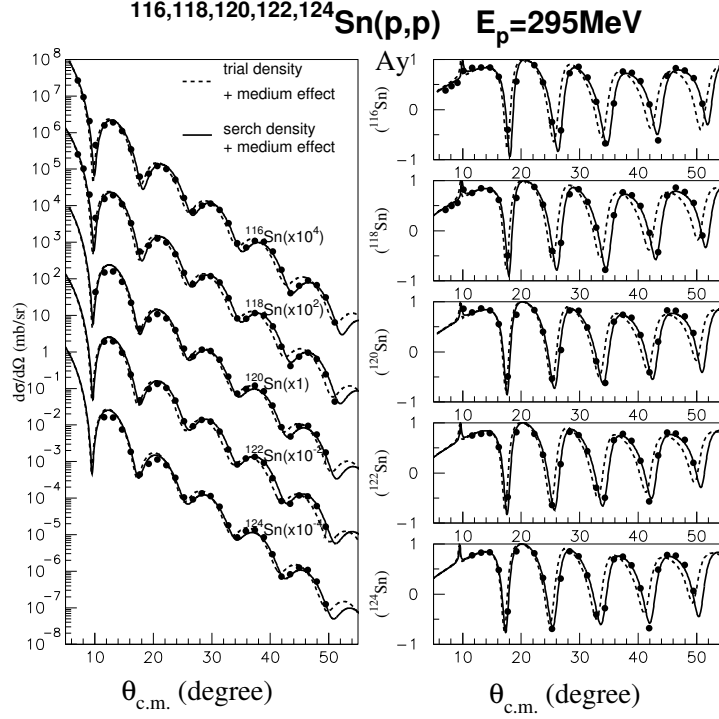

Fig.6 ^{116,118,120,122,124}Sn(p,p) data and RIA analysis

the target within 0.5 seconds and measured 3 isotopes in a single run. During the movement of the target changer the beam is stopped at the exit of the ion source. The precision of the target position reproducibility is better than 0.1 mm. Energy resolution of the beam was 200 keV in FWHM, which is due to the energy width of the beam itself, but is enough to separate elastic scattering from the inelastic peaks. Differential cross sections and the analyzing powers were measured up to the 50 degree(momentum transfer of 4.5 fm^{-1}) as shown in Fig.5. In order to deduce neutron density distributions from the scattering, we have used point proton density distribution unfolded from the charge distribution by electron scattering[ref.7]. For unfolding we used the sum of monopole type proton charge form factor obtained from the e-p scattering[ref.8]. The point proton density distribution are shown in Fig. 7 in the broken curves.
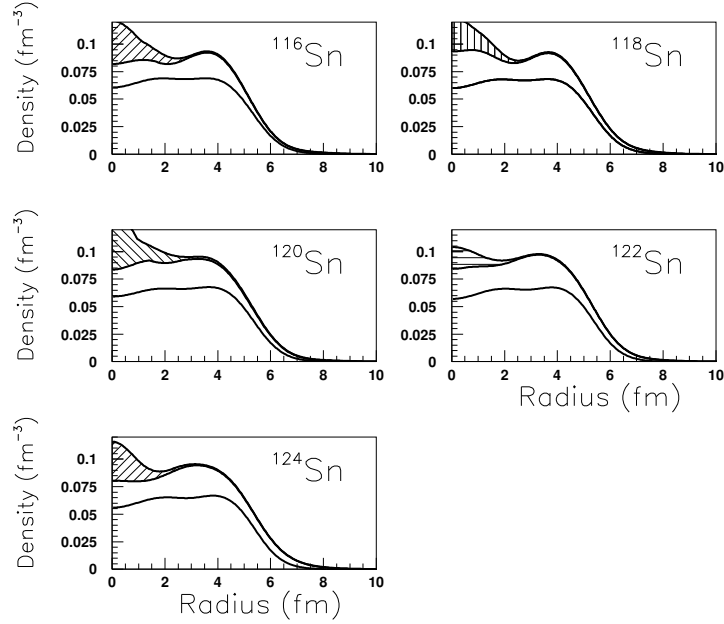
14

Fig. 7 Deduced neutron density distributions. The broken curves are point proton densities.

7 Neutron density distributions

As for the form of neutron distribution we have used sum of Gaussian type form shown as follows; For neutron density search we have used 12 parameters of N_i . Other parameters such as γ, R_i , were taken from the SOG type charge distribution by Sick[ref.6].

$$\rho_n(\mathbf{r}) = \frac{N}{2\pi^{3/2}\gamma^3} \sum_{i=1}^{12} \frac{N_i}{1 + 2R_i^2/\gamma^2} \left(e^{-(r-R_i)^2/\gamma^2} + e^{-(r+R_i)^2/\gamma^2} \right),$$

$$\sum_{i=1}^{12} N_i = 1, \quad \int \rho_n(\mathbf{r})d\mathbf{r} = N.$$

As initial densities for the search we have used 3 different forms. The set1 has a dip in the nuclear center, whereas set3 has a small bump due to the $3s_{1/2}$ orbit in the nuclear center. The set2 has the same shape as the proton distribution. In Fig.5 we show experimental data together with the results

15

of the search(shown by solid curves) and the calculations using initial set1 neutron density distributions(broken curves). As for the medium effects we have used the same parameter defined by the scattering from the ^{58}Ni target.

In Fig.8 we show the obtained neutron density distributions for tin isotopes. The error bands shown by the hatched area in the figures are defined by the contour curves of the density distributions generated by the Monte Carlo calculation with the increase of the reduced χ^2 less than the number of fitting parameters as shown in the following formula, which take into account even the ambiguities of our RIA model.

$$\chi_\nu^2 \le \chi_{\nu min}^2 + \nu \quad \chi_\nu^2 = \frac{1}{N} \sum_i \frac{(x_{calcu}^i - x_{exp}^i)^2}{\delta x_{exp}^i}$$

The point proton densities are also shown by the curves without hatched area in the same figure. In this figure we can notice only a gradual change of density due to the large ambiguity at the nuclear center. In this search and calculation we have taken into account the ambiguities of the medium effect parameters of the ^{58}Ni data and also of experimental ambiguities of the tin data by the Monte-Calro calculation. Fig. 8 displays the differences of root mean square radii between point protons and point neutron distributions. We can observe a small staggering of the difference at ^{120}Sn, which also shows the effect of the 3s$_{1/2}$ orbit filling.
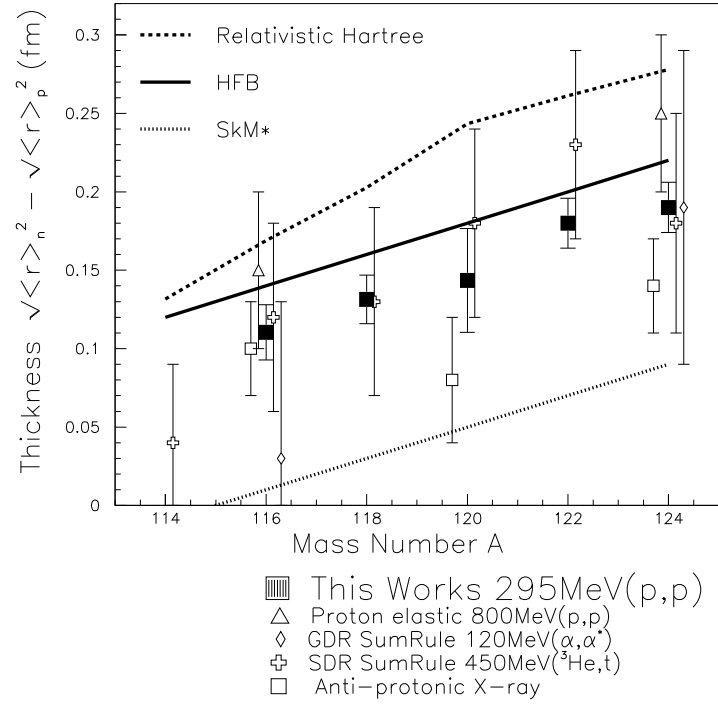
Fig. 9　Differences between proton and neutron RMS radii

8 Recoil Particle Spectrometer

Recent success of relativistic impulse approximation(RIA) to explain the proton elastic scattering from various nuclei at intermediate energies has opened a way to deduce density distribution for unstable nuclei. For unstable nuclei, various peculiar shapes of density distribution are predicted/estimated theoretically and experimentally, but until now measurements of proton elastic scattering from unstable nuclei have been performed mainly at an energy region of 30-75 MeV and would not provide direct information on the density distribution. From the experiences at IUCF, TRIUMF, LAMPF and RCNP we think that the best energy region to deduce density distribution in nuclei is between 200 MeV and 400 MeV per nucleon, where the mean free path of nucleon in nuclei is expected to be large and the scattering doesn't suffer much from the meson production. Only the new facility at RIKEN will be able to supply the sufficient unstable nuclear beam in this energy region.

8.1 How to measure elastic proton scattering for unstable nuclei

In the case of unstable nuclei we need exchange the role of the beam and the target. We use a solid hydrogen target bonbarded by the unstable nuclear beam. As is already discussed in the previous section, we are going to use intermediate energy protons in the center of mass system, namely we are going to use unstable nuclear beam of 300 MeV/A. For the measurements of the elastic scattering we are going to detect recoil protons between 70 deg. and 85 deg. in laboratory system. As a test apparatus we have constructed a recoil particle spectrometer. The detector system consists of beam line tagging system and the counter arrays to detect recoiled protons surrounding the target area. The beam line tagging system detects the scattering position at the target and gives information on the momentum and the impinging angle for each particle in the beam. The counter arrays to detect the recoiled particles are composed of drift chambers, plastic scintillators and the NaI(Tl) calorimeters in the angular region between 70 deg. and 82 deg. Since the energy of the recoiled particles strongly depends on angles as shown in the figure, the required total angular resolution is about 0.3 mrad. For the energy measurement of recoiled protons we are using NaI(Tl) scintillator at present. In the case of NaI(Tl) calorimeters the total estimated FWHM energy resolutions depends on the energy of the recoiled protons; 290 keV for the 20 MeV protons and 680 keV for the 116 MeV protons, including the effects of multiple scattering and the range struggling. Temperature control

of ±0.3deg for the calorimeter is also necessary.

Last summer we have successfully performed a test experiment to measure elastic scatterinf of 300 MeV/A oxygen 20 at heavy ion synchrotron for meadical use in Chiba near Tokyo. In the lecture new experimental data will be shown together with the proton elastic scattering data for ^{16}O and ^{18}O of Ep= 300 MeV.
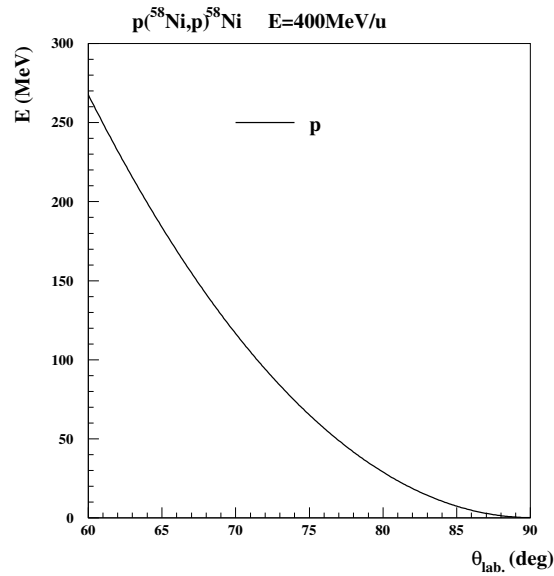

Fig.9 Kinematics of recoiled protons. Recoiled energy of protons is calculated as a function of recoil angle for the ^{58}Ni beam of $E_{58Ni}/A = 400$ MeV. In order to obtain a energy resolution of 200 keV at 70 degrees we need an angular resolution of 0.3 mrad.

19

References

[1] L. G. Arnold, B. C. Clark, R. L. Mercer and P. Schwandt, Phys. Rev. **C23**, (1981) 1949.

[2] S. Hama, B. C. Clark, E. D. Cooper, H. S. Sherif and R. L. Mercer, Phys. Rev. **C41**, (1990) 2737; E. D. Cooper, S. Hama, B. C. Clark and R. L. Mercer, Phys. Rev. **C47**, (1993) 297.

[3] J. A. McNeil, J. R. Shepard and S. J. Wallace, Phys. Rev. Lett, **50**, (1983) 1439; J. R. Shepard, J. A. McNeil and S. J. Wallace, Phys. Rev. Lett, **50**, (1983) 1443.

[4] D. P. Murdock and C. J. Horowitz, Phys. Rev. **C35**, (1987) 1442.

[5] C. J. Horowitz, Phys. Rev. **C31**, (1985) 1340.

[6] J. A. Tjon and S. J. Wallace, Phys. Rev. **C32**, (1985) 1667; Phys. Rev. **C36**, (1987) 1085.

[7] N. Ottenstein, S. J. Wallace and J. A. Tjon, Phys. Rev. **C38**, (1988) 2272.

[8] H. Sakaguchi, H. Takeda, S. Toyama, M. Itoh, A. Yamagoshi, A. Tamii, M. Yosoi, H. Akimune, I. Daito, T. Inomata, T. Noro and K. Hosono, Phys. Rev. **C57** (1998) 1749.

[9] H. V. von Geramb, *The Interaction Between Medium Energy Nucleons in Nuclei*, edited by H. O. Mayer, AIP Conf. Proc. No. 97 (AIP, New York, 1982), p. 44.

[10] L.Rikus *et al.*, Nucl. Phys. **A414**, (1984) 413; L. Rikus *et al.*, Nucl. Phys. **A426**, (1984) 496.

[11] I. Sick, Nucl. Phys. **A218**, (1974) 509; for example.

[12] H. de Vries *et al.*, Atomic Data and Nuclear Data Tables **36**, (1987) 495, and references therein.

[13] C. J. Horowitz, D. P. Murdock and B. D. Serot, *Computational Nuclear Physics 1*, (Springer-Verlag, Berlin, 1991), Chapter 7.

[14] A. Krasznahorkay, M. Fujiwara, P. van Aarle, H. Akimune, I. Daito, H. Fujimura, Y. Fujita, M. N. Harakeh, T. Inomata, J. Jänecke, S. Nakayama, A. Tamii, M. Tanaka, H. Toyokawa, W. Uijen and M. Yosoi, Phys. Rev. Lett. **82**, (1999) 3216.

[15] RCNP Annual report 1978 .

[16] H. Sakaguchi, M. Yosoi, M. Nakamura et al., *J. Phys. Soc. Japan* **55** (1986) 61.

[17] K.A. Brueckner, R.J. Eden, and N.C. Francis, *Phys. Rev.* **100** (1955) 891.

[18] ed. by H.V.v. Geramb, *Microscopic optical potential* Lecture Notes in Physics 89, Springer-Verlag Berlin(1979).

[19] F.A.Brieva and J.R. Rook, Nucl. Phys.**A291** (1977) 219, **A297** (1978) 206, **A307** (1978) 493.

[20] N. Yamaguchi, S. Nagata and T. Matsuda, *Prog. Theor. Phys.* **70** (1983) 459.

[21] N. Yamguchi, S. Nagata, J. Michiyama, *Prog. Theor. Phys.* **76** (1986) 459.

[22] S. Nagata , *Butsuri* **43** (1988) 594.

[23] N. Olsson et al., Nucl. Phys.**A472** (1987) 237.

[24] H. Sakaguchi et al.,*J. of Phys. Soc. Japan* **55**Suppl. (1986) 61.

[25] F.A. Brieva and J.R. Rook, *Nucl. Phys.* **A291**(1977)219 , 317, **A297**(1978) 206, **A307**(1978) 493.

[26] F.A. Brieva and B.Z. Georgiev, *Nucl. Phys.* **A308** (1978) 27.

[27] G. Bertsch, J. Borysowics, H. McManus, and W.G. Love, *Nucl. Phys.* **A284** (1977) 399.

[28] A.M. Green, *Phys. Lett.* **24B** (1967) 384.

[29] C.J. Horowitz, D.P. Murdoch, and B. D. Serot,*Computational Nuclear Physics 1*, Chap. 7. Springer-Verlag(1991).

[30] C.J. Horowitz and B.D. Serot, *Nucl. Phys.***A368** (1981) 503.

[31] C.J. Horowitz, *Phys. Rev.***C31**(1985) 1340.

[32] D.P. Murdock, C.J. Horowitz,*Phys. Rev.* **C35** (1987)1442.

[33] I. Sick,*Phys. Lett.***116B**(1982)212.

[34] J.A. Tjon and S.J. Wallace,*Phys. Rev.***C38** (1988) 2272.

[35] K. Kaki, **Nucl. Phys. A531** (1991) 478.

[36] H. Toki,*TMU/RIKEN Summer Institute on Unstable Nuclei*

[37] H.V. von Geramb, AIP Conf. Proc. No.97, p44.

[38] L. Rikus, K. Nakano and H.V. von Geramb, **Nucl. Phys. A414** (1984) 413; L. Rikus and H.V. von Geramb, **Nucl. Phys. A426** (1984) 496.